

RANS and DES Computations for a Wing with Ice Accretion

P. Mogili *, and D. S. Thompson †

Mississippi State University, Mississippi State, MS 39762, U.S.A

Y. Choo ‡, and H. Addy ‡

National Aeronautics and Space Administration, Cleveland, OH, 44135

A computational investigation was performed to assess the effectiveness of Detached-Eddy Simulation (DES) as a tool for predicting icing effects. The AVUS code, a public domain flow solver, was employed to compute solutions for an iced wing configuration using DES and steady Reynolds Averaged Navier-Stokes (RANS) equation methodologies. The wing section considered here was a business jet airfoil (GLC305) with a 22.5-minute glaze ice accretion (944-ice shape). The section was extruded to form a rectangular planform. The model was mounted between two walls so no tip effects were considered. The numerical results were validated by comparison with experimental data for the same configuration. The time-averaged DES computations showed some improvement in lift and drag results near stall when compared to steady RANS results. However, comparisons of the flow field details did not show the level of agreement suggested by the integrated quantities. More validation is needed to determine what role DES can play as part of an overall icing effects prediction strategy.

I. Introduction

It is well known and appreciated that the accretion of ice on lifting surfaces can significantly degrade the performance and handling characteristics of affected aircraft.¹ Less well understood, however, are the details of the complex flow fields associated with these configurations. Depending on the ice shape, these flow fields may exhibit extensive regions of unsteady separated flow. Typically, ice accretions on straight wings are categorized as "rim," "horn," or "spanwise ridge," which are more or less two-dimensional in nature, or "roughness," which is the most three-dimensional of the shapes.¹ The flow field for a horn ice accretion, which is the subject of this effort, is dominated by a separation bubble downstream of the horn. The flow separates because it is unable to recover the necessary pressure in the boundary layer after it expands around the horn. The ensuing free shear layer rolls up to form vortices that are convected downstream. The development of this unsteady flow field is critical to the resulting flow near maximum lift. The separation bubble has a large global effect and is similar to the long bubble defined by Tani.²

Many researchers have turned to computational fluid dynamics (CFD) simulations to investigate iced wing flow fields. Beginning with Potapczuk,³ numerous results from icing effects studies using the Reynolds averaged Navier-Stokes (RANS) equations have been reported in the literature. Chung, *et al.*,⁴ analyzed the flow around the ice contaminated wing surfaces of a turbo-prop aircraft. Their two- and three-dimensional analyses of a wing with a spanwise ridge accretion employed a steady RANS approach and were performed to provide insight into the aerodynamics that may have led to a loss of control of the aircraft. Reported discrepancies between the two- and three-dimensional results were attributed to a lack of grid resolution for the three-dimensional cases considered. Dunn and Loth⁵ studied the effects of simulated spanwise ice shapes on the aerodynamic performance of two-dimensional wing sections using a RANS solver developed for

*Graduate Research Assistant, Department of Aerospace Engineering, Drawer A, Student Member AIAA.

†Associate Professor, Department of Aerospace Engineering, Drawer A, AIAA Senior Member.

‡Aerospace Engineer, Icing Branch, John H. Glenn Research Center at Lewis Field, Mail Stop 11-2, Member AIAA.

unstructured meshes. A forward-facing quarter round was employed as the simulated ice shape. Additionally, they employed a solution adaptive mesh in which the mesh was refined in the separated shear layer. Their results showed that, even with adaptive mesh refinement, the pressure recovery was not correctly predicted. This discrepancy was attributed to the inability of the steady RANS simulation to model the experimentally observed unsteadiness that occurs in flow fields of this type. Pan, Loth, and Bragg⁶ performed RANS simulations for flow about airfoils with ridge ice shapes and leading edge ice shapes and compared the results to experimental data. Favorable comparisons between predicted force data and experiments were obtained up to, but not including, the stall condition, which is dominated by unsteady flow.

Recently, researchers have begun employing unsteady simulations to investigate separated flow fields. Candidate approaches for computing such unsteady flow fields include unsteady RANS (URANS), direct numerical simulation (DNS), large-eddy simulation, (LES), and detached eddy simulation (DES). Spalart⁷ contends that URANS is both "ambiguous and flawed" and that "its quantitative performance can be quite poor." DNS, while attractive from the standpoint that no modeling is required, and LES are currently impractical for realistic configurations due to their computational expense. DES, however, appears to have the potential to represent a viable near-term approach. DES is a hybrid RANS/LES approach in which a RANS turbulence model is employed in attached thin shear layers and an LES-type model is employed in regions away from the wall. This approach exploits the ability of RANS simulations to efficiently model high Reynolds number attached boundary layer flows and the ability of LES to model geometry dependent, unsteady three-dimensional flows.⁸ DES has been employed in numerous simulations of complex flow fields.^{9,10,11} DES has also been applied to the icing effects problem. Kumar and Loth¹² employed a DES technique to predict the unsteady flow around an NLF0414 airfoil section with a synthetic ice shape located on the upper surface at 3.4% chord. They also reported on computations for a rectangular three-dimensional wing using the same section. Their three-dimensional results showed some improvement relative to the steady RANS computations. Pan and Loth¹³ performed a DES for an NACA23012 airfoil with forward-facing quarter-round simulated ice accretion. Again, some improvement between the predicted results and experimental data was reported.

We previously reported results from steady RANS simulations for a horn ice shape/wing configuration.¹⁴ The basic ice shape considered was a 22.5-minute glaze ice accretion on a GLC305 airfoil, which is denoted as the two-dimensional 944-ice shape.¹⁵ The airfoil section/ice shape was extruded to form a rectangular planform wing with an aspect ratio of unity. The flow fields associated with this configuration have been studied experimentally and the results reported in the literature.^{16,17} These data include force and pressure measurements as well as mean velocity measurements and RMS fluctuations of the streamwise and transverse velocity components obtained using a split-hot-film probe. The model was mounted between the tunnel walls, so no tip effects were considered. We compared steady RANS results computed using the non-commercial version of the Cobalt₆₀ code¹⁸ (now called AVUS) with the Spalart-Allmaras turbulence model¹⁹ with the experimental data. In general, the steady RANS computations underpredicted both the lift and drag as the angle of attack was increased. Additionally, the extent of the separated region was overpredicted even at lower angles of attack. As noted above for other RANS computations, the pressure recovery was not in agreement with the experimental data. In a related effort, Chi, *et al.*²⁰ reported on the results of a series of two-dimensional steady RANS simulations for the GLC305/944-ice shape, as well as a rime ice shape, using a variety of turbulence models. The two-dimensional results for the 944-ice shape were qualitatively very similar to the three-dimensional RANS computations¹⁴ regardless of the turbulence model employed. Additionally, relatively fine meshes were employed to discretize the computational domain. Therefore, we believe the discrepancies reported by Chi, *et al.*²⁰ were not related to mesh effects.

In this paper we present the results of steady RANS computations and unsteady DES computations performed for the rectangular planform, extruded GLC305/944-ice shape wing. We first provide a brief discussion of the DES approach. Numerical considerations regarding how the mesh spacing and time step size are selected along with the mesh generation and solution procedures are discussed next. We present sample results from the two- and three-dimensional computations and compare these results with experimental data.

II. Problem Definition

The specific airfoil section considered during this effort was the GLC305 airfoil section with the 22.5-minute glaze ice accretion which is denoted as the two-dimensional 944-ice shape.¹⁵ The ice shape was extruded to form a rectangular planform wing with an aspect ratio of unity to match the configuration used

in the test program^{16,17} and is referred to here as the “extruded wing.” The airfoil model was supported horizontally across the width of the test section between two circular end-plates. These end-plates were flush mounted with the sidewalls and rotated to provide the angle of attack adjustment. Each end-plate was equipped with a porous section for sidewall boundary layer control. Numerical solutions were compared with experimental data for the following conditions: $M=0.12$, $Re/L=3.8 \times 10^6/m$ which, with a chord length of 0.9144m, yields $Re=3.5 \times 10^6$ and angles of attack from 0 deg to 6 deg in 2 deg increments. The extruded 944-ice shape cases considered here correspond to Run 41 in the experimental data.^{16,17}

III. Detached Eddy Simulation

DES was originally formulated as a modification to the Spalart-Allmaras turbulence model.^{19,8} The basic idea is to employ a RANS-type turbulence model for thin, attached shear layers and an LES model in separated regions. This approach exploits the ability of RANS simulations to efficiently model attached boundary layer flows and the ability of LES to model unsteady, geometry-dependent, three-dimensional flow fields. RANS-type models perform well for attached flows and less well for separated flows, while LES models perform well for separated flows but are prohibitively expensive to employ for computations involving thin boundary layers. We now provide a brief overview of the DES model as implemented in the Spalart-Allmaras turbulence model. More detailed discussions can be found in the literature.^{8,10,11,21}

In the Spalart-Allmaras model, the wall destruction term is taken to be proportional to $(\tilde{\nu}/d)^2$ where $\tilde{\nu}$ is a working variable related to the turbulent viscosity and d is the distance to the nearest wall. If local equilibrium occurs and the production and destruction terms are in balance, the eddy viscosity becomes proportional to $\tilde{S}d^2$ where \tilde{S} is the local strain rate. In the Smagorinsky LES model,²² the subgrid-scale turbulent viscosity is proportional to the local strain rate and the local mesh spacing squared, i.e., $\tilde{S}\Delta^2$ where $\Delta = \max(\Delta x, \Delta y, \Delta z)$. Thus, if the distance to the wall d is replaced by the local mesh spacing Δ , the Spalart-Allmaras model will locally behave like a Smagorinsky LES model. To retain the RANS-type behavior in attached boundary layers, d is replaced by a new variable $\tilde{d} = \min(d, C_{DES}\Delta)$ where C_{DES} is a constant. Note that when $d \ll C_{DES}\Delta$, the model is in a RANS mode and models the average properties of attached flow turbulence. When $d \gg C_{DES}\Delta$, the model is in LES mode and resolves eddies larger than some wavelength depending on the characteristics of the flow solved and the local mesh spacing. For unstructured meshes, the spacing Δ is taken to be the longest distance between the cell center and neighboring cell centers.²¹ The implementation of the DES model has two immediate implications regarding the mesh:

1. The mesh in the boundary layer should be highly anisotropic. In particular, the spacing along the surface should be larger than the local boundary layer thickness. This ensures that the model operates in a RANS mode near the boundary.
2. There is no advantage to having an anisotropic mesh in the interior of the domain. The premise of LES is to filter out only eddies that are statistically isotropic⁷ so that equal resolution in all directions is reasonable.

Other implications regarding the discretization of the domain are discussed in the next section.

IV. Numerical Considerations

The prediction of the aerodynamic characteristics of an iced wing is a complex problem that involves several steps. We now describe each step in some detail.

A. Geometry Modeling

The GLC305/944-ice shape definition was used as input to ICEG2D,²³ a two-dimensional tool that automates geometry modeling and mesh generation for ice accretion predictions. ICEG2D redistributes points on the upper and lower surfaces of the defined airfoil using a curvature-based equidistribution algorithm to ensure a sufficient number of points are employed in regions of the airfoil surface with high curvature. A structured surface mesh was then extruded from the section definition. This surface mesh was then converted to a meshing-ready NURBS representation using the mesh generation software GUM-B.²⁴

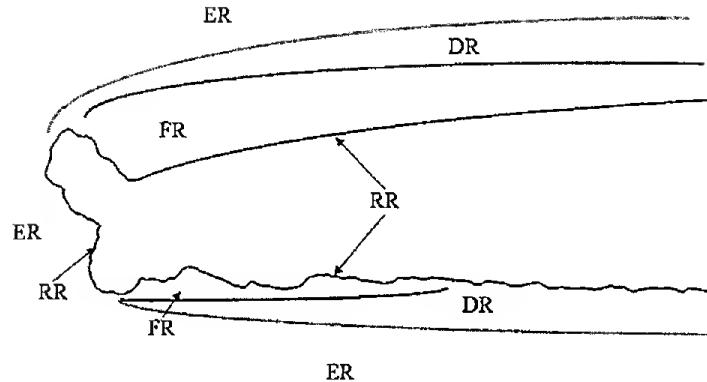


Figure 1. Estimated DES zones for GLC305 airfoil section with two-dimensional 944-ice shape (extruded wing)

B. Mesh Generation: Estimated DES Zones for an Iced Wing

It is well known that the quality of the CFD solution depends on an appropriate mesh with sufficient mesh density in regions of high flow gradients. In an unsteady separated flow dominated by convecting vortices, the vortices must be resolved adequately along with the attached boundary layers. Indeed, as noted by Spalart,⁷ “*DES compounds the gridding difficulty by incorporating both types of turbulence treatment in the same field.*” Spalart provides guidance as to how a domain should be discretized for DES modeling. He identifies several different regions with different meshing requirements:

- An **Euler region (ER)** is a region that is free of turbulence and vorticity unless it is penetrated by a shockwave. The ER covers most of the domain and an isotropic mesh can be employed in this region.
- A **RANS region (RR)** is primarily composed of the boundary layer where there is no LES content.
 - The **viscous region (VR)** is located within the RANS region and its meshing requirements are similar to those of standard RANS computations.
 - The **RANS outer region (OR)** should be discretized with a mesh in which the mesh spacing in the direction normal to the wall should not exceed once-tenth the thickness of the boundary layer. This is primarily an issue associated with numerical robustness. In practice, this rule is often violated.
- An **LES region (LR)** contains vorticity and turbulence but is not a boundary layer. Significant LES content is present in an LR.
 - The **focus region (FR)** is the region near the body in which the separated turbulence must be well resolved. The mesh should be isotropic in the FR since the LES mode filters out eddies that are statistically isotropic.
 - The **departure region (DR)** is a transitional region between the FR and the ER. The DR does not need to be resolved as well as the FR.

Here, regions are not distinguished by different equations being applied but by different priorities in the mesh spacing. An efficient mesh for any external flow can be designed with these concepts in mind, but not all are strict requirements. Figure 1 depicts the estimated DES zones discussed above as applied to the flow surrounding the 944-ice shape.

C. Selection of Mesh Spacing in Focus Region

The procedure described below follows that suggested by Spalart.⁷ According to Spalart, a well-adjusted subgrid-scale model should allow energy cascade to the smallest eddies that can be resolved on the mesh. Therefore, for most CFD solvers, an eddy with a wavelength of $\lambda = 5\Delta_o$, where Δ_o is the local mesh spacing, will be active even though it cannot be highly accurate because it lacks the energy cascade to smaller eddies,

and is under the influence of eddy viscosity instead. In other words, if we want to adequately resolve an eddy with wavelength λ , the mesh spacing should be $\Delta_0 = \lambda/5$. In the baseline mesh employed for DES computations, an eddy with a wavelength of 5% of the chord was selected, resulting in mesh spacing in the focus region of 1% of the chord. This wavelength was chosen because the height of the horn is approximately 5% of the chord. Therefore, vortices with approximately the same spatial extent as the horn height can be resolved in the separated region downstream of the horn. As part of the comparison of the DES results with experimental data, the DES mesh was refined by a factor of two in the focus region.

D. Selection of Time-Step Size

Selecting the time-step size for DES computations is challenging. Spalart¹⁹ suggests employing a local CFL number (based on the local flow velocity, the local mesh spacing, and the time step size) of unity in the focus regions (FR), that is $\frac{U_0 \Delta t}{\Delta_0} = 1$ where U_0 is the maximum flow velocity in the region. Computed RANS results indicate that the maximum flow velocity over the domain is approximately 40-50% greater than the freestream velocity. For the problem considered here with a freestream velocity of approximately 41.1m/s and a wing chord of 0.9144m, the computation for the time step size yields $\Delta t = 0.15$ ms for the baseline mesh. For the refined mesh, $\Delta t = 0.075$ ms. However, as Spalart notes,⁷ steps a factor of 3/2 or even 2 away in either direction from this estimate cannot be considered as "incorrect." Unfortunately, tests with different time steps rarely give any strong indications toward an optimal value.⁷ Thus, some ambiguity remains in the selection of the time step size. Solutions were therefore obtained on the baseline mesh using the smaller time step to test the effects of reducing the time step size for a fixed mesh.

E. Unstructured Mesh Generation

Three different meshes were generated for the extruded wing configuration: a relatively coarse mesh that was used solely for RANS computations, a baseline mesh, and a refined mesh. The coarse RANS mesh was generated using SolidMesh. SolidMesh is an interface to the unstructured surface and volume mesh generation software AFLR2 and AFLR3.²⁵ AFLR3 uses an advancing front algorithm to insert a point in the mesh. The point insertion is followed by a local reconnection to improve mesh quality. The baseline and refined meshes were generated using GridTool²⁶ and VGridns.²⁷ VGridns uses an advancing layer algorithm to generate a tetrahedral volume mesh. The near-body elements of these all-tetrahedral meshes were converted into prisms using the Blacksmith utility²⁸ thereby producing a mixed element hybrid mesh. SolidMesh produces a hybrid mesh with prisms and tetrahedra automatically. These hybrid meshes were employed because of their potential for improved efficiency and accuracy in comparison to unstructured tetrahedral meshes. The GridTool/VGridns combination was chosen for the DES meshes because it gives the user control of the point spacing on the wing surface and the flow field through the use of "sources."

Figure 2 shows two cross-sections through the refined DES mesh. Since the figure was generated using cutting planes, the line segments represent intersections of cell faces with the cutting plane. The connectivity of the mesh is evident and the tetrahedra/prism layers near the surface are clearly visible. Note the finer resolution in the focus region downstream of the horn for the refined mesh. This figure also illustrates the connection between the surface mesh and volume mesh. Because of the manner in which the mesh is generated, i.e., anisotropic tetrahedra/prisms transitioning to isotropic tetrahedra, the surface mesh characteristics are propagated into the volume mesh. Therefore, in order to refine the mesh spacing in the domain, it is necessary to refine the mesh on the surface.

Mesh refinement was obtained by reducing the magnitudes of the line sources in appropriate regions. In this case, the mesh was locally refined by reducing the source strengths in the upper surface FR by a factor of two while holding the other source strengths constant. This was found to be a reasonably efficient mechanism for mesh refinement for this problem. Since the focus of this effort was the flow on the upper surface, the lower surface mesh was made relatively coarse in comparison.

Table 1 shows statistics for the three meshes employed to generate the results reported here. Notice that the localized mesh refinement in the refined mesh produces more than a 25% increase in the number of cells when compared to the baseline mesh. In some sense, this mesh refinement can be thought of as a manual, albeit crude, attempt at solution adaptive meshing. In all cases, the distance to the first point off the wall was defined so that an average y^+ value less than 0.5 was obtained. This value is well within the recommended values for the turbulence model employed.

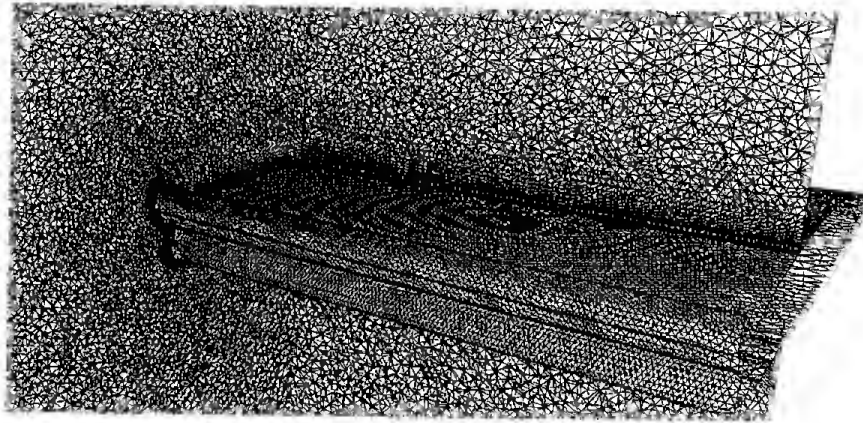


Figure 2. Refined DES mesh in cutting planes for extruded GLC305/944-ice shape (extruded wing)

Table 1. Statistics for the meshes employed in this effort

	# Nodes	# Faces	# Cells
Extruded Wing (coarse mesh)	890,958	5,299,738	2,258,447
Extruded Wing (baseline mesh)	1,828,711	17,327,367	8,341,019
Extruded Wing (refined mesh)	2,394,393	22,088,508	10,579,834

F. Flow Solution

The flow solver employed in this effort is the non-commercial version of Cobalt₆₀,²⁹ which is now called AVUS to reduce confusion with the commercial version of the flow solver. The AVUS flow solver was designed for general unstructured meshes. It employs a nonlinear Riemann solver for the inviscid flux computations and can be run either in explicit or implicit mode. Second-order spatial accuracy is obtained using a linear least-squares reconstruction of the data. The detailed computational methodology used in AVUS is described in the literature.¹⁸

All computations were performed using second-order spatial accuracy. The RANS solutions reported here were obtained using first-order, implicit local time stepping and do not in any way represent time-accurate solutions. For the DES computations, the second-order temporal integration scheme was employed. It should be noted that a CFL number of unity in the focus region yields a CFL number on the order of 100,000 in the boundary layer. Therefore, for stability reasons, it was necessary to use the fully-implicit integration scheme ($\theta = 1$) for the DES computations. Based on recommendations in the Cobalt₆₀ user's manual,²⁸ two Newton iterations, each consisting of 30 Gauss-Seidel iterations, were employed per time step. Several turbulence models are available including the Spalart-Allmaras one-equation model,¹⁹ which was used for the computations reported here. No transition point was specified, and the flow was assumed to be fully turbulent. A slip boundary condition was applied on the artificial side boundaries to reduce computational expense. This boundary condition is not believed to introduce significant error in the modeling of the flow since a porous sidewall was employed for boundary layer control in the experiment.

V. Results

In this section, we present comparisons between experimental data^{16,17} and results computed using both steady RANS and unsteady DES models. We focus first on gross flow field quantities, e.g., lift and drag coefficients. We then present comparisons of detailed flow field quantities at the midspan of the wing – the mean surface pressure distribution and field distributions of the mean streamwise velocity component and the RMS of the streamwise velocity fluctuations. We conclude with an assessment of the validity of the DES.

More details and additional comparisons are provided in Mogili³⁰ and Thompson and Mogili.³¹

Because of the associated computational expense, we have chosen to apply DES only to the 4 deg and 6 deg angle of attack cases. RANS computations were performed for angles of attack from 0 deg to 6 deg in 2 deg increments. Although the lower surface also has a region of separated flow, the flow is dominated by the large region of unsteady separated flow on the upper surface. Additionally, no field data were obtained on the lower surface during the experiments. Therefore, our discussion will focus on the region of the flow downstream of the upper surface horn.

The RANS computations were performed on three meshes – the coarse mesh, the baseline mesh, and the refined mesh – described in Table 1. The DES computations were performed on the baseline mesh and the refined mesh. The RANS simulations were initiated using an impulsive start and were continued until the normal force reached a steady state, which typically required 15,000–16,000 global iterations. The RANS solutions were then used as initial conditions for the DES computations. The sudden change in the eddy viscosity (due to the reduction in the length scale when the DES computation is initiated) represents a non-physical transient that must be eliminated. Therefore, in all cases, DES computations were performed for 0.75s (a nondimensional time of $U_\infty t/L=33.7$), which corresponds to 5000 steps for $\Delta t=0.15\text{ms}$ and 10000 steps for $\Delta t=0.075\text{ms}$ to eliminate this transient. Data was then collected during an additional 0.75s for a total nondimensional time of 67.4 beyond the steady RANS solution.

All cases reported in this effort were run on 64 processors on the EMPIRE cluster or the MAVERICK cluster at the ERC at Mississippi State University. The EMPIRE cluster is a supercomputer class cluster of workstations consisting of 1038 one GHz or better Pentium III processors each with one or more GB of RAM. The MAVERICK cluster is also a supercomputer class cluster comprised of 192 IBM x335 nodes. Each node contains dual 3.06 GHz Xeon processors and 2.5 GB of RAM. For the three-dimensional RANS solutions on the baseline mesh, 1 hour and 39 minutes were required for each 100 iterations on the EMPIRE cluster, whereas 2 hours and 23 minutes were required for each 100 iterations on the refined mesh. For the three-dimensional DES computations, 2 hours and 52 minutes were required for 100 time steps on the baseline mesh. Three hours and 52 minutes were required for each 100 time steps on the refined mesh.

A. Description of Experimental Data

Addy, *et al.*¹⁶ performed icing effects studies for the configuration of interest in this effort. The lift and pitching moment data were obtained by integrating the surface pressures, while the drag coefficients were calculated using the standard momentum deficit method based on pressures measured using a wake probe. Corrections to the integrated performance coefficients accounting for solid and wake blockage and streamline curvature were applied to the data during post processing. Broeren, *et al.*¹⁷ also carried out flow field measurements on the upper surface of the same model. Data were obtained at three different angles of attack preceding stall at Reynolds numbers of 3.5×10^6 and 6.0×10^6 and Mach numbers of 0.12 and 0.21. Split-hot-film anemometry was used to measure the time-averaged flow velocities and its RMS fluctuations.

B. Comparison of Lift and Drag Coefficients

Figure 3 shows a comparison of the predicted lift and drag coefficients with experimental data. For the DES results, the lift and drag coefficients represent mean values that were obtained using the temporal averaging procedure described above. In general, the steady RANS methodology underpredicts the lift with respect to the experimental data with the differences increasing with increasing angle of attack. Mesh refinement does not significantly improve the RANS results. The DES results show significant improvement in comparison to the steady RANS results at an angle of attack of 6 deg, irrespective of the mesh density or time step size. Less improvement is apparent at a 4 deg angle of attack. With the exception of the steady RANS results obtained on the coarse mesh, the drag coefficient comparison shows a similar trend. The steady RANS and time-averaged DES approaches underpredict the drag coefficient although the DES results show improvements relative to the RANS results. The relatively good agreement between the experimental data and the steady RANS results computed on the coarse mesh probably should be considered fortuitous since the agreement degrades as the mesh is refined.

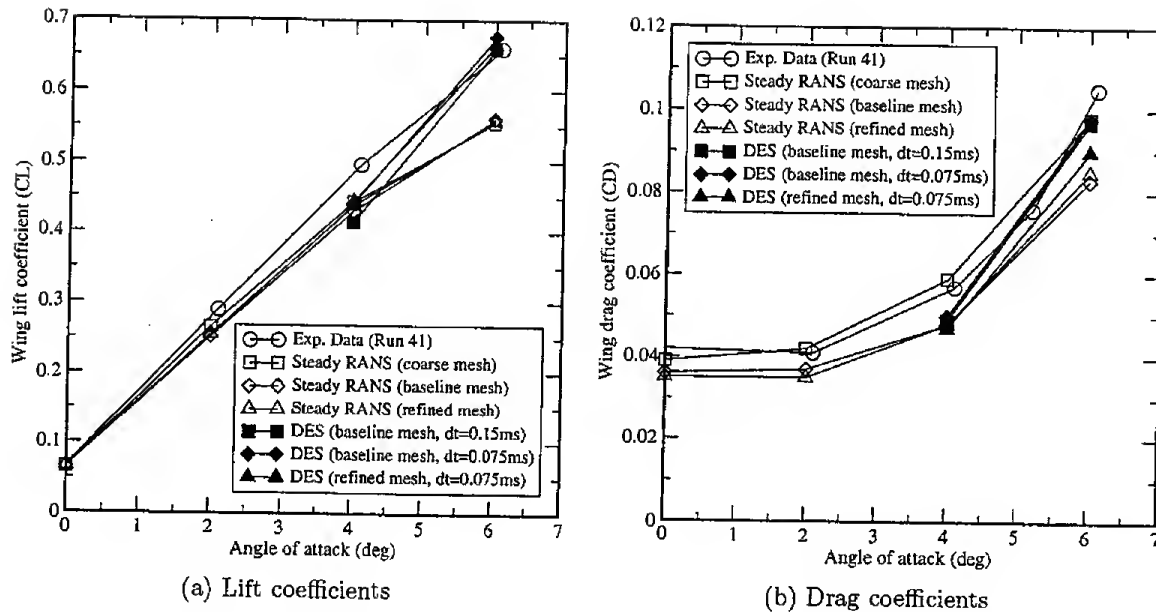


Figure 3. Comparison of predicted wing lift and drag coefficients and experimental data^{16,17}

C. Detailed Comparisons with Experimental Data

We now present comparisons of detailed flow field data for the predicted results and experimental data at angles of attack of 4 deg and 6 deg. In general, there were significant differences between steady RANS results and time-averaged DES results. The effects of spatial and temporal refinement were less significant for a given method.

Figure 4 shows a comparison of predicted results and experimentally determined time-averaged chord-wise pressure coefficient distributions at the midspan of the wing. Figure 4(a) shows comparisons between experimental data, steady RANS results, and time-averaged DES results for an angle of attack of 4 deg. In general, none of the predicted results do a very good job of reproducing the upper surface pressures downstream of the horn. The constant pressure plateau appearing just downstream of the horn in the DES results is indicative of a significant region of flow separation. The pressure plateau is less prominent in the experimental data and is not evident in the RANS results. The pressure recovery in the DES results shows an aft shift in comparison to the RANS results and better matches the experimental data. We note that, with the exception of the coarse RANS solution, spatial and temporal refinement have only minimal impact on the resulting pressure distributions. The lift values obtained by integrating the pressures appear consistent with the results observed in Figure 3.

Figure 4(b) shows the same comparisons for the 6 deg angle of attack case. Again, we note that the discrepancies between the steady RANS prediction made on the coarse mesh and the experimental data are decreased as the mesh is refined. Less influence of spatial and temporal refinement is observed for other results. The pressure plateau exhibited in each distribution suggests an extensive region of separated flow. The pressure recovery displayed in the time-averaged DES results shows better agreement with the experimental data than the results obtained from the steady RANS simulations. As evident from the plot, there is a "downward" shift of the predicted DES pressures relative to the experimental data. The shape of the pressure distribution is well predicted except on the lower surface just aft of the horn, for which the resolution may be inadequate since we chose to focus on the upper surface, and just downstream of the horn. This is particularly true for the refined mesh case. As we will note below, there is a significant secondary recirculation in the predicted results whose streamwise extent appears to coincide with the location of the differences between the predictions and the experimental data on the upper surface of the wing. The qualitative agreement between the overall shape of the time-averaged DES pressure distributions and the experimental data is encouraging as it represents an improvement when compared to the steady RANS predictions.

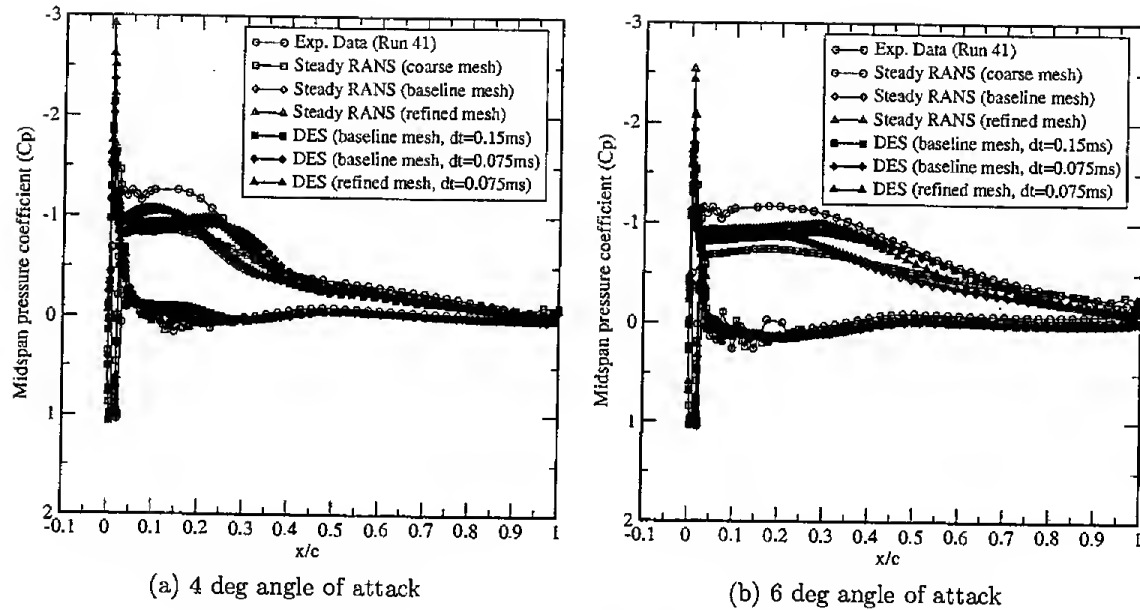


Figure 4. Comparison of predicted midspan wing pressure coefficients and experimental data

We now consider the distribution of the mean streamwise velocity in a plane parallel to the chordline at the midspan of the wing. Due to space limitations, we focus on results obtained on the refined mesh. However, the comparisons shown here are representative of those observed during the study. Figure 5(a) shows a comparison between the predicted midspan streamwise velocity contours and experimental data obtained using a hot split-film probe for the refined mesh for an angle of attack of 4 deg. The location of the reattachment of the primary upper surface flow at this spanwise position may be estimated by finding the position at which the zero streamwise velocity contour intersects the surface of the wing. From Figure 5(a), we can see that reattachment occurs at approximately 31% of the chord in the RANS results, at approximately 39% of the chord for the DES results, and approximately 28% of the chord for the experimental results. Thus, for both RANS and DES results, the predicted reattachment location is aft of the location suggested by the experimental data. This is a trend we observed for all of the computed results regardless of the methodology employed or spatial and temporal resolution. Further, the DES results show a rearward shift of the region of maximum reversed flow velocity in comparison to both the RANS results and the experimental data. Additionally, there is a significant secondary recirculation evident in the DES results just downstream of the horn (as indicated by the green region near the surface). There is a very small recirculation region in the RANS results that is not visible in Figure 5(a). Although it is likely that a recirculation of lesser extent exists in the flow field, it does not appear in the experimental data. The seemingly anomalous velocity contours that appear in the experimental data just downstream of the horn are artifacts from the process employed to generate the contour plots.

Figure 5(b) shows a comparison between the predicted midspan streamwise velocity contours and experimental data obtained using a hot split-film probe for the refined mesh for an angle of attack of 6 deg. For this case, both the RANS and DES results show a fully-separated flow on the upper surface. The experimental data suggests a reattachment location at approximately 50% chord. There is significantly more reversed flow in the RANS results in comparison to the DES results as evidenced by the thick contour of velocity in the -0.2 to 0.0 range that extends to the trailing edge in the RANS results. The RANS results also show a reversed flow velocity of larger magnitude from approximately 5% to 50% of the chord. As before, the region of maximum reversed flow is shifted aft in the predicted results relative to the experimental, more so in the DES results than in the RANS results. Again, a significant secondary recirculation is present in the DES results just downstream of the horn. Although not evident from this image, there is a smaller recirculation region present in the steady RANS results. At this angle of attack, there is a small recirculation region is barely perceptible in the experimental data.

We now consider the streamwise velocity fluctuations in the midspan plane. Figure 6(a) shows a com-

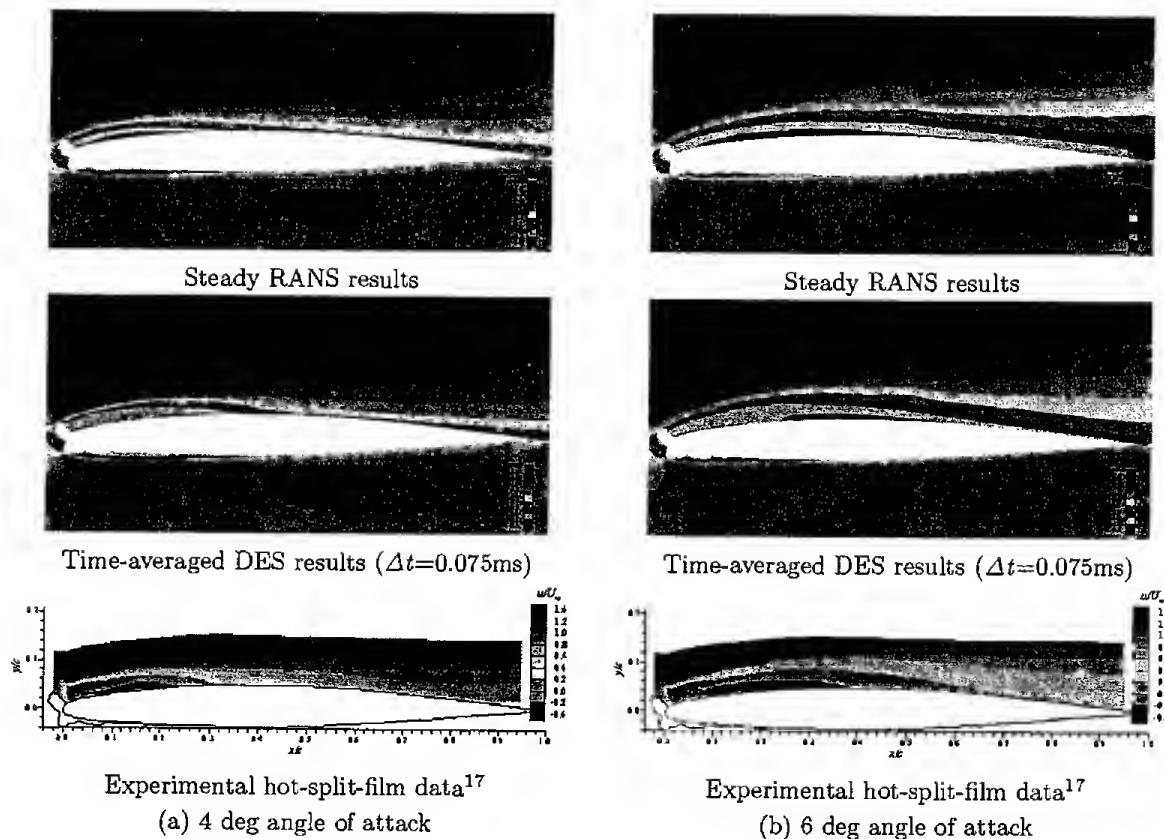


Figure 5. Comparison of predicted midspan u-velocity contours and experimental data for the extruded wing – refined mesh

parison between the RMS of the fluctuations in the streamwise velocity component predicted by the DES computation and experimental data. The turbulence intensity was calculated as the root-mean-square of the fluctuating streamwise component of velocity normalized by the freestream velocity. The fields are qualitatively similar. However, the location of the region containing the maximum fluctuations is shifted downstream. Additionally, there is a region in the predicted results just downstream of the horn that is characterized by a much lower level of fluctuations. The secondary circulation mentioned above is located in this region. These results suggests that the shear layer roll up may be delayed.

Figure 6(b) shows a comparison between the RMS of the fluctuations in the streamwise velocity component predicted by the DES computation and experimental data. The fields are qualitatively similar. However, the location of the region containing the maximum fluctuations is shifted downstream and its downstream extent is somewhat larger than that observed in the experimental data. This suggests that the predicted upper surface flow is somewhat more active than the physical flow. As before, the region of lower values of predicted fluctuations in the region just downstream of the horn suggests that the previously noted recirculation is a fairly steady phenomenon. Again, the shear layer roll up appears somewhat delayed in comparison to the experimental data.

D. Validity of DES Results

It is now useful to question the validity of the DES. In this context, validity refers to how well the DES has resolved significant features in the flow, i.e, are the spatial and temporal resolutions adequate for the problem at hand? The approach taken here is to compare solutions computed on two different meshes – the baseline and refined meshes which differ by the spacing of mesh points in the focus region – and solutions computed on the same mesh using two different time steps – the refined mesh with $\Delta t=0.15\text{ms}$ and $\Delta t=0.075\text{ms}$. Because of the complexity of the unsteady three-dimensional flow fields, the comparisons employed here are

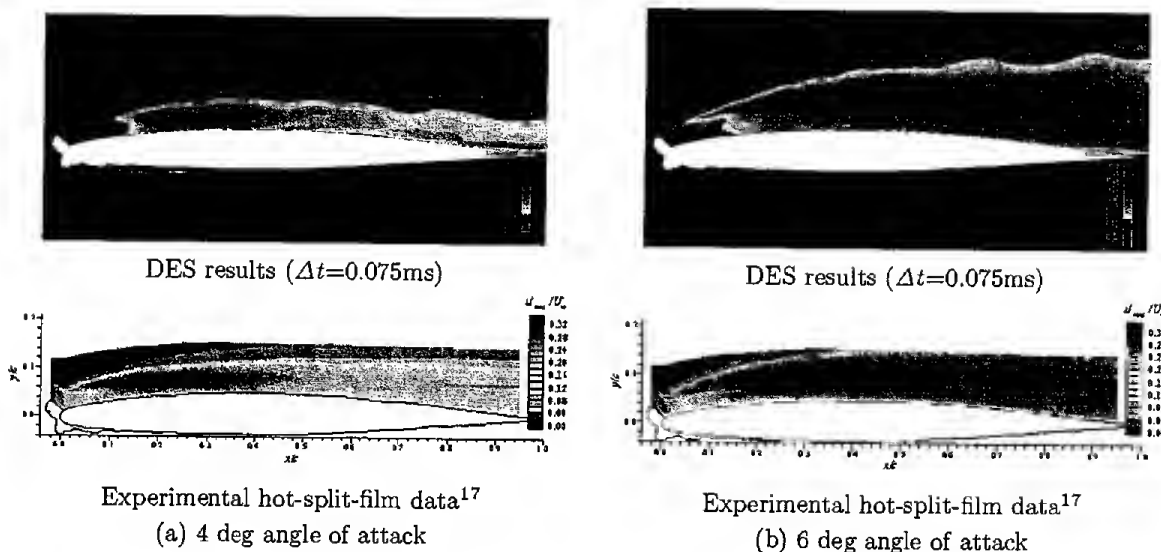


Figure 6. Comparison of the RMS of the fluctuations in the u-velocity component for the extruded wing – refined mesh

based on the lift histories. The periodogram function of MATLAB³² was used to analyze the time histories of the wing lift coefficient. The power spectral density (PSD) of the time history of the lift coefficient is computed and plotted against the frequency of the signal. Due to space limitations, we focus only on the results obtained after mesh refinement. The time interval was 0.75s to 1.5s after the initiation of the DES computation. For $\Delta t=0.075\text{ms}$, this corresponds to 10,000 time steps. For $\Delta t=0.15\text{ms}$, this corresponds to 5,000 time steps. Figure 7 shows a comparison of the PSD signatures for the three-dimensional DES solutions on the baseline and refined meshes with $\Delta t=0.075\text{ms}$ for 6 deg angle of attack. From the figure, it is apparent that similar signatures are obtained up to 15Hz. Figure 7(b), which is the zoomed version of Figure 7(a) in the frequency range 10-100Hz, shows differences above 15Hz. Similar results were obtained for the time step refinement study but with quantitative differences occurring at frequencies of approximately 12Hz.

These and similar results indicate that both the time-step refinement and mesh refinement only significantly affected the signal at frequencies higher than 12-15Hz. The power at these frequencies is at least an order of magnitude less (range 10^{-04} to 10^{-06}) than the power at the lower frequencies. Taken together with the fact that the time-averaged quantities are so similar, we can conclude that these refinements did not significantly affect the results of the simulations. Since the character of the solutions did not change with these refinements, this suggests that we have valid DES results within the context of the AVUS flow solver. This does not address the accuracy of the simulation.

We also investigated the effects of changing the number of Newton iterations employed for each time step. We performed an AVUS computation for the 6 deg angle of attack condition on the refined mesh with a time step of 0.075ms. We employed three Newton iterations instead of two. The results obtained using three Newton iterations per time step are quantitatively very similar to those obtained using two iterations. In fact, the differences were within those obtained after spatial or temporal refinement. We attribute this to the fact that we have selected a time scale that is appropriate for the problem under consideration. We also performed a PSD analysis similar to those described above. Again, we found the differences between the three iteration and two iteration cases to be similar to the differences that were observed for spatial and temporal refinement.

VI. Conclusion

The problem of flow field simulation for iced wing configurations is a complex one that severely taxes existing capabilities for geometry modeling, mesh generation, and flow solution. Particularly challenging are

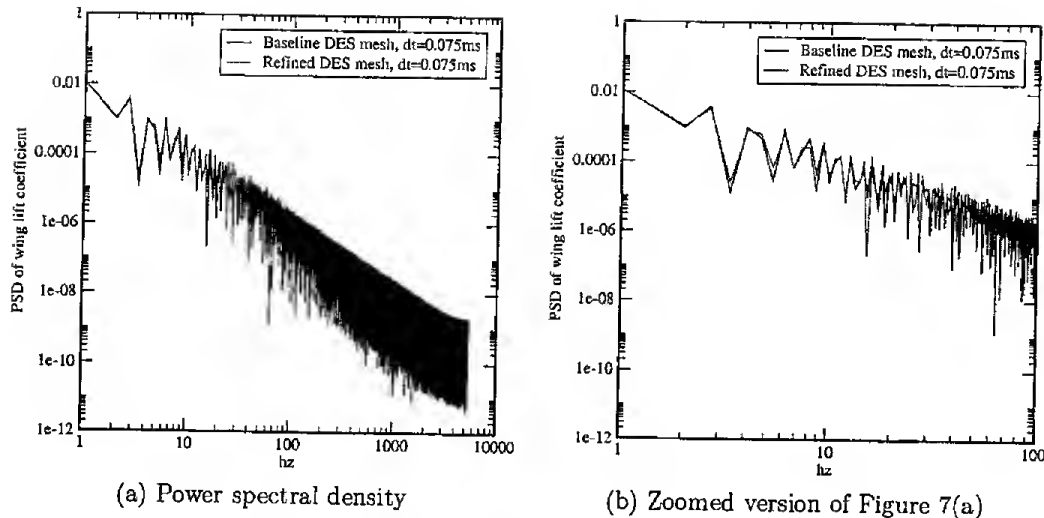


Figure 7. Comparison of power spectral density plots for baseline mesh and refined mesh at 6 deg angle of attack, with $\Delta t=0.075\text{ms}$

cases in which there are regions of unsteady flow separation. In this context, the effectiveness of Detached-Eddy Simulation (DES) as a tool for predicting icing effects was evaluated. The AVUS code was employed to compute solutions for an iced wing configuration using DES and steady Reynolds Averaged Navier-Stokes (RANS) equation methodologies. The configuration was an extruded GLC305/944-ice shape section with a rectangular planform. The model was mounted between two walls so no tip effects were considered. The numerical results were validated by comparison with experimental data for the same configuration.

The benefits of employing three-dimensional DES computations are not clear at this time. The time-averaged DES computations did show improvement in lift and drag results at an angle of attack of 6 deg when compared to steady RANS results. Similar agreement was not obtained at an angle of attack of 4 deg. Comparisons of detailed flow field quantities such as surface pressure distribution and the mean streamwise flow velocity distribution did not show the level of agreement suggested by the integrated quantities. In particular, DES results showed more extensive flow separation than the experimental data. Further, the DES results showed a significant secondary recirculation that was not present in the experimental data. The DES results also exhibited a delayed shear layer roll up.

Based on our results, we believe that DES may prove useful in a limited sense to provide analysis of iced wing configurations when there is significant flow separation, e.g., near stall, where steady RANS computations are demonstrably ineffective. However, more validation is needed to determine what role DES can play as part of an overall icing effects prediction strategy.

VII. Acknowledgment

This effort was supported by NASA GRC (NAG3-2562 and NAG3-2892) with Yung Choo as Technical Monitor. We would like to extend our appreciation to Stuart Pope of NASA LRC for his assistance with GridTool and Matthew Grismer of AFRL for his assistance with the AVUS flow solver. We would also like to thank Andy Broeren of UIUC for his helpful discussions relating to the experimental data. Thanks are also due Mithun Varma of MSU who assisted with the images and Satish Chalasani who generated the coarse mesh.

References

- ¹Bragg, M. B., Broeren, A. P., and Blumenthal, L. A., "Iced-Airfoil and Wing Aerodynamics," *SAE*, June 2003.
- ²Tani, I., *Low Speed Flows Involving Bubble Separations*, Pergamon, New York, 1964.
- ³Potapczuk, M., "Numerical Analysis of an NACA0012 Airfoil with Leading Edge Ice Accretions," 1987, AIAA Paper 87-0101.

- ⁴Chung, J., Choo, Y., Reehorst, A., Potapczuk, M., and Slater, J., "Navier-Stokes Analysis of the Flowfield Characteristics of an Ice Contaminated Aircraft Wing," 1999, AIAA Paper 1999-0375.
- ⁵Dunn, T. A. and Loth, E., "Effects of Simulated-Spanwise-Ice Shapes on Airfoils: Computational Investigation," 1999, AIAA Paper 1999-0093.
- ⁶Pan, J., Loth, E., and Bragg, M. B., "RANS Simulations of Airfoils with Ice Shapes," 2003, AIAA Paper 2003-0729.
- ⁷Spalart, P. R., "Young-Persons Guide to Detached-Eddy Simulation Grids," Tech. Rep. NASA CR-2001-211032, NASA, July 2001.
- ⁸Spalart, P. R., Jou, W. H., Strelets, M., and Allmaras, S. R., "Comments on the Feasibility of LES for Wings, and on a Hybrid RANS/LES Approach," *Advances in DNS/LES, 1st AFOSR International Conference on DNS/LES*, August 1997.
- ⁹Forsythe, J. R., Squires, K. D., Wurtzler, K. E., and Spalart, P. R., "Detached-Eddy Simulation of Fighter Aircraft at High Alpha," 2002, AIAA Paper 2002-0591.
- ¹⁰Morton, S. A., Forsythe, J. R., Squires, K. D., and Wurtzler, K. E., "Assessment of Unstructured Grids for Detached Eddy Simulation of High Reynolds Number Separated Flows," *Proceedings of the 8th International Conference on Numerical Grid Generation in Computational Field Simulations*, Honolulu, June 2002.
- ¹¹Squires, K. D., Forsythe, J. R., Morton, S. A., Strang, W. Z., Wurtzler, K. E., Tomaro, R. F., Grismer, M. J., and Spalart, P. R., "Progress on Detached-Eddy Simulation of Massively Separated Flows," 2002, AIAA Paper 2002-102.
- ¹²Kumar, S. and Loth, E., "Detached Eddy Simulations of an Iced-Airfoil," 2001, AIAA Paper 2001-0678.
- ¹³Pan, J. and Loth, E., "Detached Eddy Simulations for Airfoil with Ice Shapes," 2004, AIAA Paper 2004-0564.
- ¹⁴Thompson, D., Mogili, P., Chalasani, S., Addy, H., and Choo, Y., "A Computational Icing Effects Study for a Three-Dimensional Wing: Comparison with Experimental Data and Investigation of Spanwise Variation," 2004, AIAA Paper 2004-056.
- ¹⁵Addy, H., "Ice Accretions and Icing Effects for Modern Airfoils," Tech. Rep. NASA TP-2000-210031, NASA, April 2000.
- ¹⁶Addy, H., Zoeckler, J., and Broeren, A., "A Wind Tunnel Study of Icing Effects on a Business Jet Airfoil," 2003, AIAA Paper 2003-0727.
- ¹⁷Broeren, A., Addy, H. E., and Bragg, M. B., "Flowfield Measurements about an Airfoil with Leading-Edge Ice Shapes," 2004, AIAA Paper 2004-0559.
- ¹⁸Strang, W. Z., Tomaro, R. F., and Grismer, M. J., "The Defining Methods of Cobalt60: A Parallel, Implicit, Unstructured Euler/Navier-Stokes Flow Solver," 1999, AIAA Paper 1999-0786.
- ¹⁹Spalart, P. R. and Allmaras, S. R., "A One-Equation Turbulence Model for Aerodynamic Flows," *La Recherche Aerospaciale*, Vol. 1, 1994, pp. 5-21.
- ²⁰Chi, X., Zhu, B., Shih, T. I.-P., Addy, H. E., and Choo, Y., "CFD Analysis of the Aerodynamics of a Business Jet Airfoil with Leading-Edge Ice Accretion," 2004, AIAA Paper 2004-0560.
- ²¹Forsythe, J. R., Hoffmann, K. A., and Dietiker, J. F., "Detached Eddy Simulation of a Supersonic Axisymmetric Base Flow with an Unstructured Solver," 2000, AIAA Paper 2000-2410.
- ²²Smagorinsky, J., "General Circulation Experiments with the Primitive Equations. I. The Basic Experiments," *Mon. Weather Rev.*, Vol. 91, 1963, pp. 99-164.
- ²³Thompson, D. and Soni, B., "ICEG2D: A Software Package for Ice Accretion Prediction," 2003, AIAA Paper 2003-1070.
- ²⁴Jiang, M. and Remotigue, M., "GUM-B Grid Generation Code and Applications," *Numerical Grid Generation in Computational Field Simulations, Proceedings of the 6th International Conference*, London, England, July 1998.
- ²⁵Marcum, D., *Handbook of Grid Generation*, J. F. Thompson, B. K. Soni, and N. Weatherill, eds, chap. Unstructured Grid Generation using Automatic Point Insertion and Local Reconnection, CRC Press, Boca Raton, FL, 2nd ed., 1998.
- ²⁶Samareh, J., "GridTool: A Surface Modeling and Grid Generation Tool, Proceedings of the Workshop on Surface Modeling, Grid Generation, and Related Issues in CFD Solutions," Tech. Rep. NASA CP-3291, NASA, May 1995.
- ²⁷Pirzadeh, S., "Three-Dimensional Unstructured Viscous Grids by the Advancing Layers Method," *AIAA Journal*, Vol. 34, No. 1, January 1996, pp. 43-49.
- ²⁸Strang, W. Z., *Cobalt60: User's Manual*, September 2000.
- ²⁹Tomaro, R. F., Strang, W. Z., and Sankar, L. N., "An Implicit Algorithm for Solving Time Dependent Flows on Unstructured Meshes," 1997, AIAA Paper 1997-0333.
- ³⁰Mogili, P., *RANS and DES Computations for Wings with Ice Accretions*, Master's thesis, Mississippi State University, August 2004.
- ³¹Thompson, D. and Mogili, P., "Detached-Eddy Simulations of Separated Flow around Wings with Ice Accretions: Year 1 Report (NAG3-2892)," Tech. rep., NASA GRC, September 2004.
- ³²<http://www.mathworks.com/>.